

Systematic Control of the Interlayer Exchange Coupling in Perpendicularly Magnetized Synthetic Antiferromagnets

Teng Xu^{1,2}, Jiahao Liu,^{1,2} Xichao Zhang³, Qihan Zhang,^{1,2} Heng-An Zhou,^{1,2} Yiqing Dong,^{1,2} Pierluigi Gargiani,⁴ Manuel Valvidares⁴, Yan Zhou,⁵ and Wanjun Jiang^{1,2,*}


¹State Key Laboratory of Low-Dimensional Quantum Physics and Department of Physics, Tsinghua University, Beijing 100084, China

²Frontier Science Center for Quantum Information, Tsinghua University, Beijing 100084, China

³Department of Electrical and Computer Engineering, Shinshu University, 4-17-1 Wakasato, Nagano 380-8553, Japan

⁴ALBA Synchrotron Light Source, Cerdanyola del Vallès, 08290 Barcelona, Spain

⁵School of Science and Engineering, The Chinese University of Hong Kong, Shenzhen, Guangdong 518172, China

 (Received 12 June 2022; revised 17 August 2022; accepted 28 September 2022; published 16 November 2022)

The interlayer exchange coupling (IEC) in synthetic antiferromagnets (SAFs) is attracting considerable attention in the spintronics community. While exciting physics is revealed, systematic control of the IEC via tuning the thickness of the magnetic layer is yet to be adequately addressed in SAFs with perpendicular magnetic anisotropy (PMA). In this work, we experimentally investigate this aspect in Pt/Co/Ru/Fe_{0.55}Tb_{0.45} [ferromagnet (FM)/Ru/ferrimagnet (FIM)] multilayers with PMA, which possess a broader material-parameter space beyond what can be achieved with traditional SAFs. More importantly, the incorporation of the Fe-Tb FIM layer into the SAF multilayers allows us to directly probe the layer-resolved magnetization reversal by utilizing the anomalous Hall effect and standard magnetometry measurements. Our findings are further verified by x-ray magnetic circular dichroism measurements by providing element-resolved magnetic behaviors. Moreover, through systematic control of the IEC, IEC-modulated SAFs with different magnetization reversal behaviors can be acquired, which is further studied by performing magnetic simulations. Our results suggest that systematic control of the IEC through tuning the thickness of FIM layers can be achieved in FM/Ru/FIM multilayers, which could be useful for designing SAF-based magnetic memory and sensing devices.

DOI: [10.1103/PhysRevApplied.18.054051](https://doi.org/10.1103/PhysRevApplied.18.054051)

I. INTRODUCTION

Understanding and implementing the interlayer exchange coupling (IEC) in magnetic multilayers have led to the discovery of many exciting opportunities for realizing spintronic phenomena and devices [1]. For example, the observation of giant magnetoresistance and synthetic antiferromagnets (SAFs) is closely correlated to the IEC, which typically occurs between two ferromagnetic layers that are separated by a nonmagnetic spacer [2–5]. In the standard ferromagnet_B/nonmagnet/ferromagnet_T (FM_B/NM/FM_T) SAFs, the IEC is in the form of the oscillatory Ruderman-Kittel-Kasuya-Yosida (RKKY) interaction, which originates from the spatial oscillations of spin density in the NM spacer [6–8]. The oscillating spin density leads to an IEC that oscillates with the thickness of the NM spacer, which results in FM and antiferromagnetic (AFM) couplings [9–11]. SAFs possess

a reduced stray field and high thermal stability due to strong IEC and can be electrically manipulated as standard FM layers [4]. Towards a functional spin-orbitronic device, SAFs with perpendicular magnetic anisotropy (PMA) are widely employed in spin valves and magnetic tunneling junctions [12–20] and demonstrate the accommodation of rich innovative phenomena [21–27].

In standard SAFs with PMA, such as Co/Ru/Co and Co/Ir/Co, the thickness of the NM spacer (Ru and Ir) is generally limited (in the range of 1–2 nm) [28–31]. Its ability to control the IEC is thus reduced to a relatively narrow thickness range. On the other hand, theoretical calculations show that the thickness of the FM layer can equivalently modulate the strength of the RKKY interaction [32–40]. This modulation can be attributed to the multiple reflections of electrons in the FM layers [32–36]. Thus, it affects the resultant electronic density in the NM spacers caused by the adjacent ferromagnets [41–43]. Specifically, by varying the thickness of the FM layer, both the strength and sign of the RKKY interaction can be further tuned,

*jiang_lab@tsinghua.edu.cn

which can serve as another tuning knob for controlling both the sign and amplitude of the IEC [44,45].

The thickness of the FM layer can influence the IEC, which has been previously investigated in standard SAF structures (such as Co-Fe-B/Pt/Ru/Pt/Co-Fe-B and Co-Fe-B/Ta/Co-Fe-B) with PMA [46,47]. The thickness range in these studies is, however, rather limited due to the interfacial origin of PMA in the involved multilayers [48,49]. Note that the reduced interfacial PMA and AFM IEC generally lead to canted magnetizations in both FM layers [46,47]. Therefore, implementing a magnetic film with a bulk PMA over a wide thickness range is not only important for designing versatile SAF structures but also can largely advance SAF-based spintronics.

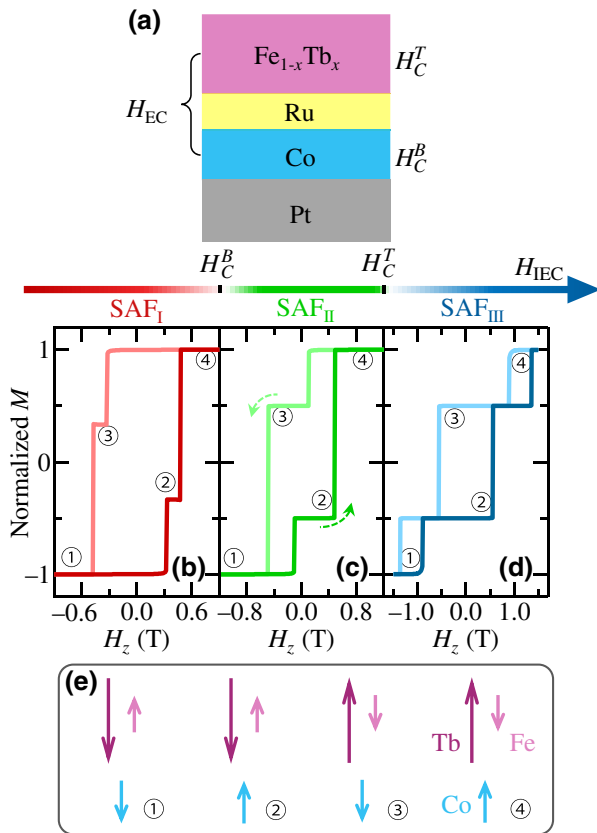


FIG. 1. (a) Schematic illustration of Pt/Co/Ru/Fe-Tb SAF multilayer. (b)–(d) Simulated magnetic hysteresis loops of three typical SAFs (SAF_I, SAF_{II}, SAF_{III}) by engineering the effective field of the interlayer exchange coupling, H_{IEC} . Dark and light colors represent the ascending and descending branches of the whole sweeping loop, respectively. Directions of the dotted-line arrows indicate the direction of sweeping. (e) Four typical magnetization configurations of parallel (① and ④) and antiparallel (② and ③) alignments of (net) magnetic moments of the Co and Fe-Tb magnetic layers. Blue arrows denote magnetization of the Co layer. Dark- and light-pink arrows represent magnetizations of the Tb and Fe sublattices, respectively.

Here, we study the evolution of the IEC in the Pt/Co/Ru/Fe-Tb multilayer by replacing the FM layer with a Fe_{0.55}Tb_{0.45} FIM layer of different thicknesses, while maintaining PMA [shown in the Fig. 1(a)]. Furthermore, by comparing the effective field of IEC (H_{IEC}) with the coercive field (H_C) of the involved magnetic layers, various SAFs with different magnetization reversal behaviors are present. In particular, a rich phase diagram of SAFs is established. It should be emphasized that the layer-resolved magnetization configurations in the present system can be studied by performing anomalous Hall effect (AHE), magnetometry, and element-specific x-ray magnetic circular dichroism (XMCD) measurements, while in the fully compensated magnetization state ($M_z = 0$). This aspect cannot be easily done in standard SAFs, such as Co/Ru/Co and Co/Ir/Co multilayers [50].

II. EXPERIMENTS

Magnetic multilayers Ta(1)/Pt(3)/Co(t_{Co})/Ru(t_{Ru})/Fe_{0.55}Tb_{0.45}(t_{Fe-Tb})/SiN_x(5) (number denotes the thickness in nanometers) are fabricated on thermally oxidized silicon substrates by using an ultrahigh vacuum magnetron sputtering system (AJA Orion 8). The base pressure of the main chamber is better than 1×10^{-8} Torr and the Ar pressure is 3 mTorr. A 1-nm-thick Ta is used as an adhesive layer and a SiN_x(5) layer is used to prevent oxidation. The Fe-Tb FIM layers are synthesized by cosputtering of the Fe and Tb targets, in which the atomic ratio can be adjusted by fixing the growth power of the Fe target while changing the growth power of the Tb target. Note that the composition of Fe_{0.55}Tb_{0.45} (atomic ratio) is fixed throughout the present work. Five series of samples: Ta(1)/Pt(3)/Co(1.2)/Ru(t_{Ru})/Fe_{0.55}Tb_{0.45}(6.0)/SiN_x(5), Ta(1)/Pt(3)/Co(1.2)/Ru(1.1)/Fe_{0.55}Tb_{0.45}(t_{Fe-Tb})/SiN_x(5), Ta(1)/Pt(3)/Co(t_{Co})/Ru(1.1)/Fe_{0.55}Tb_{0.45}(6.0)/SiN_x(5), Ta(1)/Pt(3)/Co(t_{Co})/Ru(1.1)/Fe_{0.55}Tb_{0.45}(3.6)/SiN_x(5), and Ta(1)/Pt(3)/Co(0.5)/Ru(1.1)/Fe_{0.55}Tb_{0.45}(t_{Fe-Tb})/SiN_x(5) are synthesized. Magnetometry measurements are performed by utilizing a superconducting quantum interference device magnetometer, together with a vibrating sample magnetometer. The AHE measurements are carried out by using a home-built electrical transport measurement system. The element-specific x-ray absorption spectroscopy (XAS) and XMCD magnetometry measurements are conducted at the Co $L_{2,3}$, Fe $L_{2,3}$, and Tb $M_{4,5}$ edges at the BOREAS beamline of the ALBA Synchrotron Light Source [51]. All measurements are performed at room temperature.

In the rare-earth–transition-metal (RE-TM) FIM with a composition of Fe_{0.55}Tb_{0.45}, the 4*f* electrons of the RE (Tb) elements are localized; hence, electrical transport behavior is dominated by the TM (Fe) spin sublattice

[52–54]. In Tb-dominated $\text{Fe}_{0.55}\text{Tb}_{0.45}$ layers, magnetization of the Tb element (\vec{m}_{Tb}) is parallel with the external perpendicular field (H_z), while that of the Fe element (\vec{m}_{Fe}) is antiparallel with the H_z . The AHE loop thus exhibits an opposite sign compared to the results from magnetometry measurements, since the latter measures the net magnetization (M_z) between the Tb and Fe sublattices. Thus, the AHE measurements can be utilized to directly distinguish the order of magnetization reversal of the Co and Fe-Tb layers [50].

III. RESULTS AND DISCUSSION

A. Microscopic understanding of the magnetization configuration in SAFs

In the standard $\text{FM}_B/\text{NM}/\text{FM}_T$ trilayer, where $\text{FM}_{B(T)}$ denotes the bottom (top) FM layer, the sign of IEC can be tuned from the FM (positive) to AFM coupling (negative) by varying the thicknesses of the FM and/or NM layers [33,45]. In particular, the magnetization configurations of SAFs can be studied by minimizing the Zeeman, anisotropy, IEC energy, and intralayer exchange energy [47,55], which reads as

$$\begin{aligned} E_{\text{tot}} = & -\mu_0(M_S t_T \vec{H}_z \cdot \vec{m}_T + M_S t_B \vec{H}_z \cdot \vec{m}_B) \\ & - K_{u,T} t_T (\vec{m}_T \cdot \hat{e}_z)^2 - K_{u,B} t_B (\vec{m}_B \cdot \hat{e}_z)^2 \\ & + J_{\text{IEC}} (\vec{m}_T \cdot \vec{m}_B) - A_{\text{intra},T} (\nabla \vec{m}_T)^2 \\ & - A_{\text{intra},B} (\nabla \vec{m}_B)^2. \end{aligned} \quad (1)$$

Here, μ_0 is the vacuum permeability. $M_{S,T(B)}$, $K_{u,T(B)}$, $A_{\text{intra},T(B)}$, and $t_{T(B)}$ are the saturation magnetization, magnetic anisotropy, intralayer exchange constant, and thickness of the top (bottom) FM layer, respectively. Here, $\vec{m}_{T(B)}$ and \hat{e}_z are the normalized net magnetization vectors of the top (bottom) FM layer and the unit vector normal to the film plane, respectively. The negative (positive) IEC energy constant (J_{IEC}) determines the occurrence of the antiparallel (AFM) [parallel (FM)] magnetization configuration. A micromagnetic study of the $\text{FM}_B/\text{Ru}/\text{FM}_T$ trilayer is conducted by using the Mumax3 software, with the aim of examining the role of the IEC strength in tuning the magnetization dynamics. The micromagnetic simulations are performed by numerically integrating the Landau-Lifshitz-Gilbert equation. Detailed descriptions can be found in part 1 of the Supplemental Material [56]. Specifically, the out-of-plane magnetic anisotropy, K_u , adopted in the simulations is 350 kJ m^{-3} for FM_B and 200 kJ m^{-3} for FM_T [57–61].

Through systematically examining the strength of the IEC fields (H_{IEC}) and the coercive fields of the top (H_C^T)

and bottom (H_C^B) FM layers, various SAFs with different magnetization reversal behaviors are first categorized. Specifically, if the value of H_{IEC} is smaller than both H_C^T and H_C^B ($H_{\text{IEC}} < H_C^T < H_C^B$ or $H_{\text{IEC}} < H_C^B < H_C^T$), we identify this as SAF_I , which exhibits a two-step magnetization reversal. The simulated M - H_z loop (red curve) is shown in Fig. 1(b). It can be seen that a fully compensated magnetization is absent at zero field ($H_z = 0$) in SAF_I with a small IEC. Note that the SAF_I is quite different from the magnetically decoupled bilayers where the top and bottom FM layers exhibit an independent response to H_z .

When the exchange field, H_{IEC} , is larger than the coercive field of the bottom FM layer (which exhibits a smaller H_C^B), but smaller than the top FM layer ($H_C^B < H_{\text{IEC}} < H_C^T$), a two-step magnetization reversal (green curve), shown in Fig. 1(c), can also be observed. Through sweeping $-H_z$ to $+H_z$, the magnetization (\vec{m}_B) of the bottom FM layer switches first (before $H_z = 0$), and that of the top FM layer (\vec{m}_T) flips subsequently following the increase of H_z . Note that another type-II SAF_{II} can be identified if H_{IEC} is larger than the coercive field of the top FM layer (H_C^T) but smaller than that of the bottom FM layer (H_C^B). In this case ($H_C^T < H_{\text{IEC}} < H_C^B$), magnetization of the top FM layer (\vec{m}_T) reverses before $H_z = 0$. For comparison, SAFs with the above magnetization reversal behaviors are marked as SAF_{II} .

Following a continuous increase of H_{IEC} , the strength of H_{IEC} can be larger than coercive fields of both FM layers ($H_C^B < H_C^T < H_{\text{IEC}}$ or $H_C^T < H_C^B < H_{\text{IEC}}$). In this case, a three-step magnetization reversal (blue curve) can be observed, which is labeled as SAF_{III} , as shown in Fig. 1(d). In the ascending branch of the hysteresis loop, the bottom (or top) FM layer flips first before $H_z = 0$. An increase of H_z leads to the simultaneous switching of the top and bottom FM layers, as a result of the strong AFM coupling (H_{IEC}). A further increase of H_z (larger than H_{IEC}) results in an alignment of both FM layers along the direction of H_z . It should be emphasized here that an antiparallel state ($M_z = 0$) can only be achieved in SAF_{II} and SAF_{III} at $H_z = 0$ due to the onset of strong AFM exchange coupling. Thus, through increasing the strengths of IEC, $\text{SAF}_{I,II,III}$ with different magnetization reversal behaviors can be resolved. The corresponding four typical magnetization configurations, including parallel and antiparallel alignments, are schematically illustrated in Fig. 1(e). Considering the variation of magnetic anisotropy, K_u , additional micromagnetic simulations are conducted and listed in part 1 of the Supplemental Material [56]. It is found that the variation of K_u alone cannot substantially alter the dynamics of SAFs, implying the important role of IEC. Note that these IEC-modulated SAFs ($\text{SAF}_{I,II,III}$) were previously observed in $\text{FM}/\text{NM}/\text{FM}$ SAFs via tuning the thickness of the NM spacer layer [30,62], but not by the thickness of the FM layer, which is studied in the present work.

B. Experimental realization of SAFs with tunable IEC

In the following part, we experimentally realize systematic control of the IEC in Pt/Co/Ru/Fe-Tb multilayers, via tuning the thickness of the Co and Fe-Tb layers. Through optimizing the thickness of the Ru spacer (1.1 nm in our case), we have previously studied the fully compensated SAF Pt/Co/Ru/Fe-Tb/SiN_x multilayers with a pronounced AHE and magneto-optical responses [50]. Systematic control of the IEC via tuning the thickness of magnetic layers was, however, not demonstrated in that work, but is studied here. In Ta(1)/Pt(3)/Co(1.2)/Ru(t_{Ru})/Fe-Tb(6.0)/SiN_x(5) multilayers, the RKKY-mediated IEC can be easily tuned from FM ($J_{\text{IEC}} > 0$) to AFM ($J_{\text{IEC}} < 0$) coupling through changing the Ru spacer thickness, t_{Ru} . The effective field of the AFM IEC, H_{IEC} , can be determined by minor-loop measurements [50].

To realize SAF_I with a small IEC, systems with a variable thickness of Ru spacer (t_{Ru}) are studied, while fixing the thicknesses of the Co and Fe-Tb layers. When the Ru spacer is 2.0 nm, a two-step magnetization reversal can be observed in the Pt/Co(1.2)/Ru(2.0)/Fe-Tb(6.0) multilayer, as shown in part 2 of the Supplemental Material [56]. The strength of the IEC is estimated from a small shift of the minor loops of the Co layers from the origin ($H_z = 0$). This indicates the presence of a small IEC coupling, which

leads to an independent switching of the top and bottom layers. Note that an antiparallel state cannot be realized at $H_z = 0$ in SAF_I due to the weak IEC.

In the range of $1.0 \text{ nm} \leq t_{\text{Ru}} \leq 1.4 \text{ nm}$, different magnetization behaviors, which are similar to SAF_{II}, can be realized in Pt/Co(1.2)/Ru(t_{Ru})/Fe-Tb(6.0) multilayers [50]. With t_{Ru} fixed at 1.1 nm, we investigate SAF_{II} and SAF_{III} by changing the thicknesses of the Co and Fe-Tb layers (t_{Co} and $t_{\text{Fe-Tb}}$). The evolution of coercive fields with varying thicknesses of Co and Fe-Tb layers can be found in part 3 of the Supplemental Material [56]. As shown in Fig. 2(a), a two-step magnetization reversal can be observed with the Fe-Tb thickness in the range of $4.5 \text{ nm} \leq t_{\text{Fe-Tb}} \leq 6.0 \text{ nm}$. This is qualitatively consistent with the simulated SAF_{II} with a larger IEC. The low remanent moments at the synthetic AFM states are determined by the (net) magnetic moments of the Co (\vec{m}_{Co}) and Fe-Tb ($\vec{m}_{\text{Fe-Tb}}$) layers. Note that SAF_{II} can also be realized by varying the thickness of the Co layer ($0.8 \text{ nm} < t_{\text{Co}} < 1.2 \text{ nm}$) in the Pt/Co(t_{Co})/Ru(1.1)/Fe-Tb(6.0) multilayers with a fixed thickness of the Fe-Tb layer, as shown in Fig. 2(b).

Utilizing magnetometry measurements, the IEC can be successfully controlled in SAF_{II} by choosing different Co and Fe-Tb layers, in which two different cases, $H_C^{\text{Co}} < H_{\text{IEC}} < H_C^{\text{Fe-Tb}}$ or $H_C^{\text{Fe-Tb}} < H_{\text{IEC}} < H_C^{\text{Co}}$, can be realized.

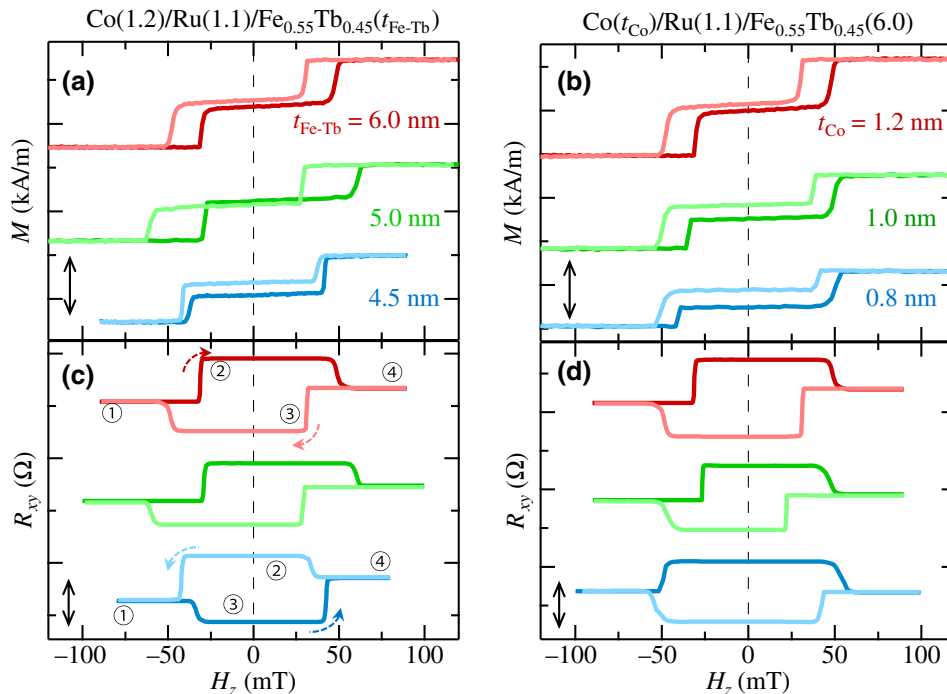


FIG. 2. Experimental realization of SAF_{II} by changing the thickness of Fe-Tb and Co layers. (a),(b) M - H_z loops of SAF_{II}, Pt/Co(1.2)/Ru(1.1)/Fe-Tb($t_{\text{Fe-Tb}}$)/SiN_x and Pt/Co(t_{Co})/Ru(1.1)/Fe-Tb(6.0)/SiN_x, with different thicknesses of Fe-Tb and Co layers. Scale bar is 300 kA/m. (c),(d) Corresponding AHE loops. Dark and light colors represent ascending and descending branches, which are indicated by the dotted arrows in (c), respectively. Scale bar is 1.0 Ω . Numbers represent the magnetization configurations in Fig. 1(e).

However, the order of layer-dependent reversal cannot be directly identified from magnetometry data, as shown in Figs. 2(a) and 2(b), respectively. In the following, we reveal the order of layer-dependent magnetization reversal by performing AHE measurements.

Shown in Figs. 2(c) and 2(d) are the AHE loops of the Pt/Co(1.2)/Ru(1.1)/Fe-Tb($t_{\text{Fe-Tb}}$) and Pt/Co(t_{Co})/Ru(1.1)/Fe-Tb(6.0) multilayers, respectively. In the case of the thick Fe-Tb and Co layers ($4.5 \text{ nm} \leq t_{\text{Fe-Tb}} \leq 6.0 \text{ nm}$ or $0.8 \text{ nm} \leq t_{\text{Co}} \leq 1.2 \text{ nm}$), the presence of a two-step magnetization reversal is confirmed. The opposite sign of the AHE loops is expected between the Co layer and the Tb-rich Fe-Tb layers. Thus, in Pt/Co(1.2)/Ru(1.1)/Fe-Tb(6.0) SAF_{II}, the ascending branch of the AHE loop [dark-red line in Fig. 2(c)] demonstrates that magnetization of the bottom Co layer (\vec{m}_{Co}) first reverses at $H_z = -30 \text{ mT}$ (before zero field). With a further increase of H_z to $+50 \text{ mT}$, magnetization of the top Fe-Tb FIM layers ($\vec{m}_{\text{Fe-Tb}}$) subsequently flips. In SAF_{II}, the AFM IEC field, H_{IEC} , is smaller than the coercive field, $H_C^{\text{Fe-Tb}}$, of Fe-Tb but larger than that of the Co layer ($H_C^{\text{Co}} < H_{\text{IEC}} < H_C^{\text{Fe-Tb}}$). Similar behavior of magnetization reversal is also identified in the Pt/Co($0.8 \text{ nm} \leq t_{\text{Co}} \leq 1.2 \text{ nm}$)/Ru(1.1)/Fe-Tb(6.0) multilayer, as shown in Fig. 2(d).

With the thickness of the Fe-Tb layer fixed at 4.5 nm, magnetization of the top Fe-Tb ($t_{\text{Fe-Tb}} = 4.5 \text{ nm}$) layer ($\vec{m}_{\text{Fe-Tb}}$) first reverses at $H_z = -31 \text{ mT}$ (before zero field), and magnetization of the bottom Co layer (\vec{m}_{Co}) flips at $H_z = +40 \text{ mT}$ [dark-blue line in Fig. 2(c)]. In this case, H_{IEC} is smaller than the coercive field, H_C^{Co} , of the Co layer but larger than that of the Fe-Tb layer ($H_C^{\text{Fe-Tb}} < H_{\text{IEC}} < H_C^{\text{Co}}$). Note that R_{xy} is dominated by the magnetic moments (\vec{m}_{Co}) of the Co layer and Fe (\vec{m}_{Fe}) sublattice of the Fe-Tb layer in the current SAF structures [50]. As a result, additive AHE resistances (R_{xy}) can be achieved at the remanent states (② and ③), while reduced R_{xy} can be observed at the saturated states (① and ④). Thus, SAF_{II} exhibits a pronounced AHE response, even at the fully compensated AFM state, which is due to the incorporation of Tb-dominated FIM Fe-Tb layers.

Through continuously reducing the thickness of the Fe-Tb and Co layers, a three-step magnetization reversal is observed. This is consistent with the predicted behavior of SAF_{III} with a boosted IEC. Shown in Figs. 3(a) and 3(b) are hysteresis loops of Pt/Co(1.2)/Ru(1.1)/Fe-Tb ($t_{\text{Fe-Tb}} = 4.0, 3.2$) and Pt/Co($t_{\text{Co}} = 0.6, 0.5$)/Ru(1.1)/Fe-Tb(6.0) multilayers, respectively. In this case, the strength of the AFM

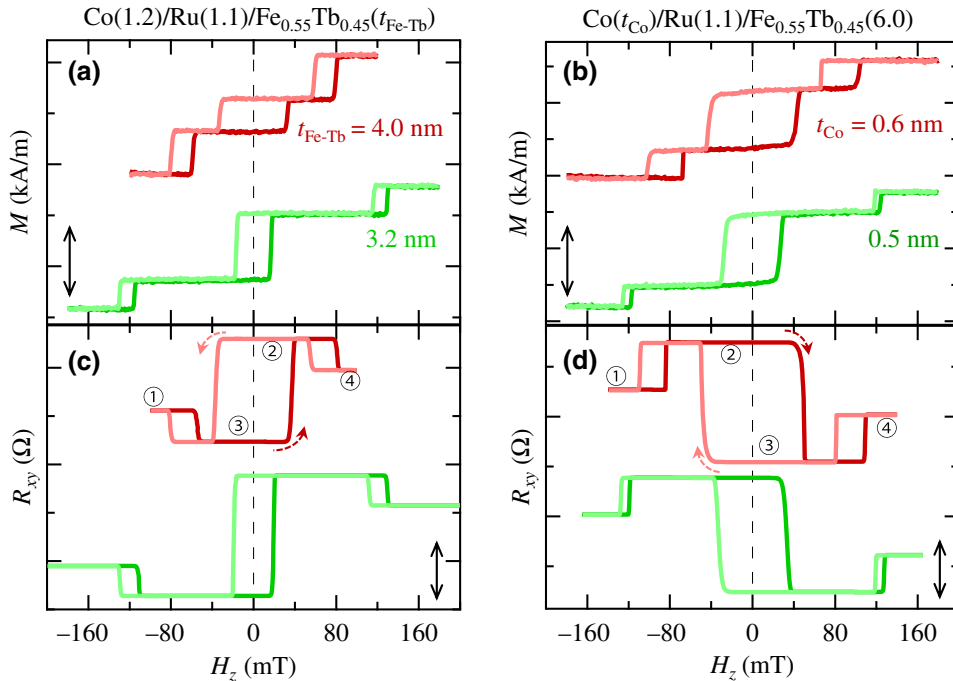


FIG. 3. Experimental realization of SAF_{III} by changing the thickness of the Fe-Tb and Co layers. (a),(b) M - H_z loops of SAF_{III}, Co(1.2)/Ru(1.1)/Fe-Tb($t_{\text{Fe-Tb}}$) and Co(t_{Co})/Ru(1.1)/Fe-Tb(6.0), with $t_{\text{Fe-Tb}} = 4.0, 3.2$ and $t_{\text{Co}} = 0.6, 0.5$, respectively. Scale bar is 300 kA/m. (c),(d) Corresponding AHE loops. Dark and light colors represent the ascending and descending branches of the whole sweeping loop, which are indicated by arrows in (c) and (d), respectively. Scale bar is 0.8 Ω . Numbers represent the magnetization configurations in Fig. 1(e).

IEC (H_{IEC}) is much greater than that of $H_C^{\text{Fe-Tb, Co}}$ ($H_C^{\text{Fe-Tb}} < H_C^{\text{Co}} < H_{\text{IEC}}$ or $H_C^{\text{Co}} < H_C^{\text{Fe-Tb}} < H_{\text{IEC}}$). We note that the fully compensated SAF_{III} at zero field can be achieved through tuning the chemical composition of $\text{Fe}_{1-x}\text{Tb}_x$ FIM layers. The order of magnetization reversal in these SAF_{III} is subsequently revealed from AHE measurements.

Figures 3(c) and 3(d) display the corresponding AHE loops of Pt/Co(1.2)/Ru(1.1)/Fe-Tb ($t_{\text{Fe-Tb}} = 4.0, 3.2$) and Pt/Co($t_{\text{Co}} = 0.6, 0.5$)/Ru(1.1)/Fe-Tb(6.0) multilayers, respectively. The expected three-step magnetization reversal, together with the layer-resolved magnetization reversion in SAF_{III}, are further verified. For instance, in Pt/Co(1.2)/Ru(1.1)/Fe-Tb(4.0) SAF_{III}, the magnetization, $\vec{m}_{\text{Fe-Tb}}$, of the Fe-Tb layer reverses at $H_z = -60$ mT in the ascending branches [dark-red line in Fig. 3(c)]. A continuous increase of H_z enables \vec{m}_{Co} and $\vec{m}_{\text{Fe-Tb}}$ to be simultaneously flipped at $H_z = +40$ mT. This can be attributed to the strong H_{IEC} of SAF_{III}. At higher external fields ($H_z \geq +80$ mT) larger than both $H_C^{\text{Co, Fe-Tb}}$ and H_{IEC} , the directions of \vec{m}_{Co} and $\vec{m}_{\text{Fe-Tb}}$ are aligned along with H_z . In Pt/Co(1.2)/Ru(1.1)/Fe-Tb(4.0) SAF_{III}, H_{IEC} is larger than both coercive fields ($H_C^{\text{Co, Fe-Tb}}$). In this multilayer, H_C^{Co} is larger than $H_C^{\text{Fe-Tb}}$, which gives rise to $H_C^{\text{Fe-Tb}} < H_C^{\text{Co}} < H_{\text{IEC}}$. The other case of the type-III SAF_{III} ($H_C^{\text{Co}} < H_C^{\text{Fe-Tb}} < H_{\text{IEC}}$), in which the Co layer first reverses before zero field, is also identified in Pt/Co($t_{\text{Co}} = 0.6, 0.5$)/Ru(1.1)/Fe-Tb(6.0) SAF_{III}, as shown in Fig. 3(d).

Since the Fe-Tb FIM film exhibits a bulk PMA, we examine the influence of the Fe-Tb thickness on the strength of IEC. Note that this aspect cannot be determined in traditional Co-based SAFs that exhibit an interfacial PMA. Additional Pt/Co(1.2)/Ru(1.1)/Fe-Tb($t_{\text{Fe-Tb}}$) SAF_{III} with various thicknesses ($t_{\text{Fe-Tb}} = 3.7, 3.5, 3.0, 2.7$ nm) can be found in the Part 4 of the Supplemental Material [56]. In Fig. S4(b) within the Supplemental Material, minor loops are measured, which enables the estimation of H_{IEC} of the SAF_{III} to be made [56]. Figure 4 summarizes the evolution of H_{IEC} as a function of the thickness of the FIM Fe-Tb and FM Co layers ($t_{\text{Fe-Tb}}$) in Pt/Co(1.2)/Ru(1.1)/Fe-Tb($t_{\text{Fe-Tb}}$) and Pt/Co(t_{Co})/Ru(1.1)/Fe-Tb(6.0) SAFs, respectively. Compared with the case of the Co layer, a substantial modulation of the IEC field (H_{IEC}) can be achieved by changing the thickness of the Fe-Tb layer. In particular, $H_{\text{IEC}} = 320$ mT is observed at $t_{\text{Fe-Tb}} = 2.7$ nm. This value is much larger than those reported in other multilayers, including Co-Fe-B/Pt/Ru/Pt/Co-Fe-B ($H_{\text{IEC}} = 200$ mT) [63], Co/Pd/Co/Ru/Co/Pd/Co ($H_{\text{IEC}} = 200$ mT) [29], Co/Pt/Ru/Pt/Co ($H_{\text{IEC}} = 100$ mT) [64], Co/Ir/Co ($H_{\text{IEC}} = 50$ mT) [65], and Co-Fe-B/Ta/Co-Fe-B ($H_{\text{IEC}} = 20$ mT) [47]. The IEC energy constant can be subsequently estimated [10,66,67]:

$$|J_{\text{IEC}}| = \mu_0 H_{\text{IEC}} M_S t_{\text{Co(Fe-Tb)}}. \quad (2)$$

Here, M_S and $t_{\text{Co(Fe-Tb)}}$ are the saturation magnetization determined by magnetometry measurements and the layer thickness of the biased Co (Fe-Tb) layer, respectively. The evolution of the IEC energy constant is shown in Fig. 4, which increases from 0.038 to 0.079 mJ/m² following variation of the IEC field, H_{IEC} .

The properties of the Pt/Co(0.5)/Ru(1.1)/Fe-Tb($t_{\text{Fe-Tb}}$) and Pt/Co(t_{Co})/Ru(1.1)/Fe-Tb(3.6) multilayers are also investigated. Their corresponding magnetization configurations are directly obtained from the AHE measurements, as shown in Figs. 5(a) and 5(b). In Pt/Co(0.5)/Ru(1.1)/Fe-Tb($t_{\text{Fe-Tb}}$), AHE loops with three-step jumps can be observed when the Fe-Tb layer thickness ranges from 6.0 to 3.2 nm, which is consistent with the simulated SAF_{III} with a much larger IEC. The evolution of the IEC field, H_{IEC} , and energy constant, J_{IEC} , as a function of the thickness of the Co (t_{Co}) and Fe-Tb ($t_{\text{Fe-Tb}}$) layers is summarized in Fig. 5(c).

Following the increased thickness of Fe-Tb layers ($t_{\text{Fe-Tb}}$), the value of H_{IEC} also increases. The IEC energy constant, J_{IEC} , also increases following the increased AFM IEC fields, H_{IEC} . In Pt/Co(t_{Co})/Ru(1.1)/Fe-Tb(3.6) multilayers, the SAF_{III} with a much larger IEC ($H_C^{\text{Fe-Tb}} < H_C^{\text{Co}} < H_{\text{IEC}}$) can be resolved in the case of $t_{\text{Co}} > 0.6$ nm. At $t_{\text{Co}} = 0.6$ nm, we observe a magnetization reversal behavior that is consistent with SAF_{II}, in which the top Fe-Tb layer first reverses at $H_z = -67$ mT ($H_C^{\text{Fe-Tb}} < H_{\text{IEC}} < H_C^{\text{Co}}$). At $t_{\text{Co}} = 0.5$ nm, SAF_{III} reappears, in which the Co layer first flips at $H_z = -75$ mT ($H_C^{\text{Co}} < H_C^{\text{Fe-Tb}} < H_{\text{IEC}}$). It is found from Fig. 5(b) that SAF_{II} is achieved by

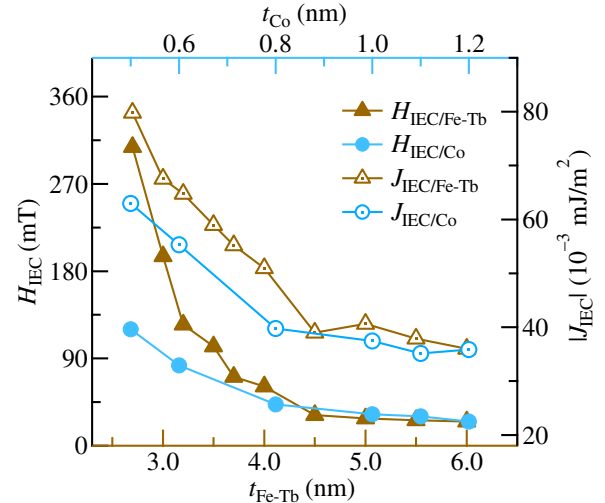


FIG. 4. Evolution of antiferromagnetic interlayer exchange field, H_{IEC} , and energy constant, J_{IEC} , as a function of the thickness of Fe-Tb ($t_{\text{Fe-Tb}}$) and ferromagnetic Co (t_{Co}) layers in Co(1.2)/Ru(1.1)/Fe-Tb($t_{\text{Fe-Tb}}$) and Co(t_{Co})/Ru(1.1)/Fe-Tb(6.0) SAFs.

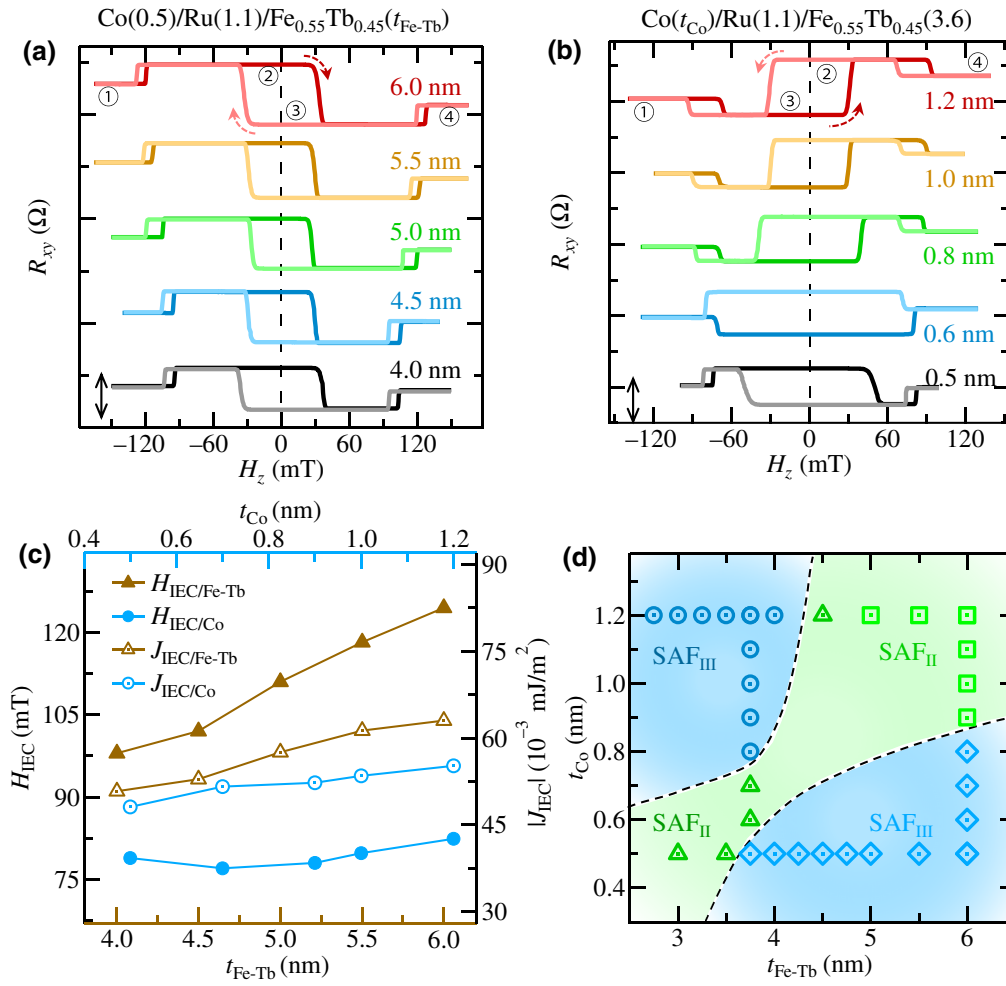


FIG. 5. AHE loops of Co(0.5)/Ru(1.1)/Fe-Tb($t_{\text{Fe-Tb}}$) (a) and Co(t_{Co})/Ru(1.1)/Fe-Tb(3.6) SAFs (b). Scale bar is 1.0 Ω . Numbers represent the magnetization configurations in Fig. 1(e). (c) Effective field of IEC, H_{IEC} , and energy constant, J_{IEC} , as a function of the thickness of Fe-Tb ($t_{\text{Fe-Tb}}$) and Co (t_{Co}) layers. (d) Summarized phase diagram for SAFs with different thicknesses of Fe-Tb ($t_{\text{Fe-Tb}}$) can Co (t_{Co}) layers. Dashed black lines are for guidance only.

changing the thickness of the Co layer, which results in a smaller H_{IEC} (~ 77 mT) than that of SAF_{III}. This is consistent with the simulations shown in Fig. 1. Summarized in Fig. 5(d) is the phase diagram of SAF_{II,III} with the tunable IEC, which is realized by tuning the thickness of the Co (t_{Co}) and Fe-Tb ($t_{\text{Fe-Tb}}$) layers.

Magnetization and transport measurements are used to indirectly infer the relative magnetization configurations of the Co and Fe-Tb layers. Below, we exploit the element-specific XMCD technique to directly study the magnetization orientation of the Co, Fe, and Tb magnetic lattices. Magnetic fields are generated by a superconducting vector cryomagnet (Scientific Magnetics), in a direction collinear with the incoming x-ray direction and normal to the sample plane. This measurement geometry enables the perpendicular magnetization (i.e., projection along the beam direction) to be probed. To obtain the spin-averaged XAS and XMCD spectra, the absorption signals

are measured as a function of the photon energy with directions of photon spin parallel $\mu_+(E)$ and antiparallel $\mu_-(E)$ to the perpendicular magnetization of Pt/Co/Ru/Fe-Tb SAF multilayers.

Figure 6(a) shows the element-specific XMCD hysteresis loops of the Co, Fe, and Tb elements that are obtained in Pt/Co(1.2)/Ru(1.1)/Fe-Tb(5.0) SAF_{II}. The ascending-field branches of the hysteresis loop for the Co element [top panel of Fig. 6(a)] indicate that the Co moment, \vec{m}_{Co} , reverses before $H_z = 0$ due to the onset of the AFM IEC. Under increased applied field, H_z , the Tb and Fe moments (\vec{m}_{Tb} and \vec{m}_{Fe}) flip simultaneously, as shown in the middle and bottom panels of Fig. 6(a). The element-specific XMCD results are consistent with the corresponding AHE and magnetometry measurements shown in Fig. 6(b). Note that the strong antiparallel alignment between the Fe and Tb elements in the Fe-Tb film is verified by revealing the absence of the spin-flop transition in the measured

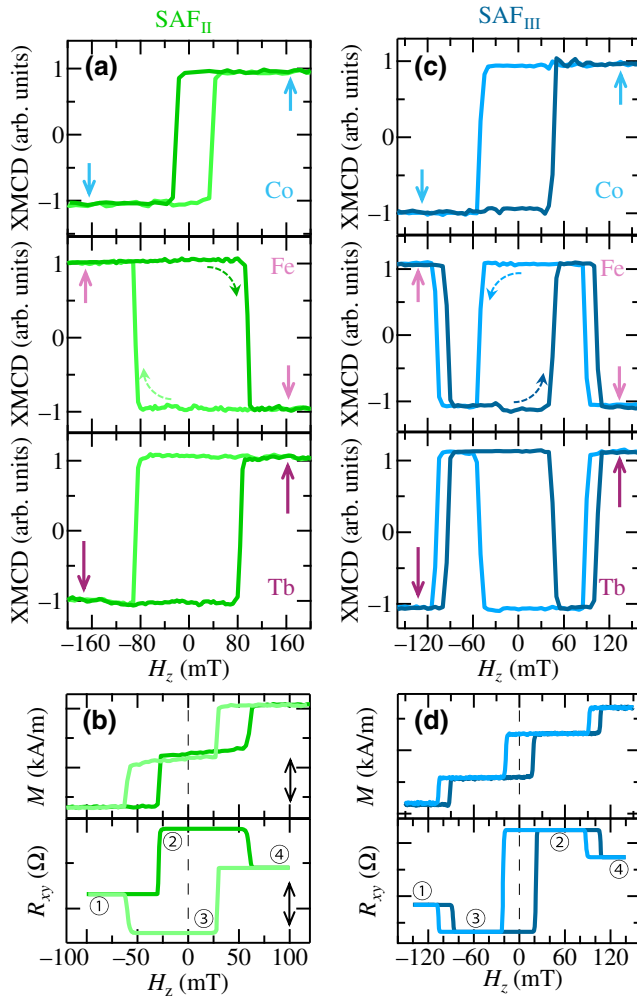


FIG. 6. Normalized element-specific XMCD magnetic hysteresis loops of Co, Fe, and Tb elements in Co(1.2)/Ru(1.1)/Fe-Tb(5.0) SAF_{II} (a) and Co(1.2)/Ru(1.1)/Fe-Tb(3.5) SAF_{III} (c), which are acquired at Co L_3 , Fe L_3 , and Tb M_5 edges, respectively. Dotted arrows denote the sweeping order of H_z . Blue arrows denote magnetization of the Co layer. Dark- and light-pink arrows represent magnetization of Tb and Fe sublattices, respectively. Corresponding $M-H_z$ and AHE loops for Co(1.2)/Ru(1.1)/Fe-Tb(5.0) SAF_{II} (b) and Co(1.2)/Ru(1.1)/Fe-Tb(3.5) SAF_{III} (d). Scale bar is 150 kA/m and 0.8 Ω . Numbers represent typical magnetization configurations in Fig. 1(e).

field range (< 200 mT). Since the signs of XMCD signals directly probe the direction of magnetization, one can conclude that magnetization of the Co layer is antiparallel to that of the Tb spin sublattice but parallel to that of the Fe spin sublattice at the SAF states.

Corresponding XMCD measurements for the case of Pt/Co(1.2)/Ru(1.1)/Fe-Tb(3.5) SAF_{III} with a much larger IEC are shown in Fig. 6(c). The XMCD hysteresis loops of the Fe and Tb sublattices exhibit similar three-step characteristics to the AHE and magnetometry measurements

shown in Fig. 6(d). The Fe-Tb and Co layers simultaneously reverse at $H_z = \pm 45$ mT because of the stronger AFM IEC between the Fe-Tb and Co layers, which is consistent with the electrical transport measurements.

IV. CONCLUSIONS

By varying the thickness of the Co and Fe_{0.55}Tb_{0.45} layers, we systematically study the evolution of the IEC in Pt/Co/Ru/Fe-Tb multilayers with perpendicular magnetic anisotropy. The IEC can be systematically controlled by tuning the thickness of magnetic layers in the present material system. Through comparing the coercive fields of the Co and Fe-Tb layers, versatile SAFs with different magnetization reversal behaviors, together with a rich phase diagram of SAFs, are successfully demonstrated. The choice of Fe-Tb (Tb-dominated) ferrimagnet allows us to directly identify layer-resolved magnetization reversals in these SAFs by utilizing conventional anomalous Hall effect measurements. Our results are further confirmed by performing XMCD magnetometry measurements. Multilevel magnetic states and controllable IECs are established in the proposed perpendicular Pt/Co/Ru/Fe-Tb SAFs, which can be desirable for magnetic memory and sensing applications. Additionally, comparable spin-orbit torques (SOTs) are revealed in single FIM layers, and thus, more efficient magnetization switching of perpendicular Pt/Co/Ru/Fe-Tb SAFs is expected through intermixing the bulk SOT in a single FIM and interfacial SOT from heavy metals [54,68–70]. Furthermore, the occurrence of interlayer Dzyaloshinskii-Moriya interactions is demonstrated in perpendicularly magnetized SAF systems and the orthogonally magnetized Co/Pt/Fe-Tb trilayer [25,26,71]. In the present Pt/Co/Ru/Fe-Tb SAFs, the correlation of the (possible) interlayer DMI and the tunable interlayer coupling strength could also be a valuable direction for future investigations.

ACKNOWLEDGMENTS

Work carried out at Tsinghua University is supported by the National Natural Science Foundation of China (Grants No. 52271181, No. 12225409, No. 51831005, No. 1181101082, and No. 11804182), the Basic Science Center Project of the NSFC (Grant No. 51788104), the Beijing Natural Science Foundation (Grant No. Z190009), the Beijing Advanced Innovation Center for Future Chip (ICFC). We acknowledge beamtime at ALBA synchrotron via official ID2019023358 and inhouse ID2018093184 proposals. X.Z. is an International Research Fellow of the Japan Society for the Promotion of Science (JSPS) and supported by JSPS KAKENHI (Grant No. JP20F20363). Y.Z. acknowledges support by the Guangdong Special Support Project (Grant No. 2019BT02X030), Guangdong Basic and Applied Basic Research Foundation (Grant No. 2021B1515120047),

the Shenzhen Fundamental Research Fund (Grant No. JCYJ20210324120213037), the Shenzhen Peacock Group Plan (Grant No. KQTD20180413181702403), the Pearl River Recruitment Program of Talents (Grant No. 2017GC010293), and the National Natural Science Foundation of China (Grants No. 11974298 and No. 61961136006). M.V. and P.G. acknowledge additional funding by grants PID2020-116181RB-C32, FlagEra SOgraphMEM PCI2019-111908-2 (AEI/FEDER).

-
- [1] A. Hrabec, Z. Luo, L. J. Heyderman, and P. Gambardella, Synthetic chiral magnets promoted by the Dzyaloshinskii–Moriya interaction, *Appl. Phys. Lett.* **117**, 130503 (2020).
- [2] M. N. Baibich, J. M. Broto, A. Fert, F. N. Van Dau, F. Petroff, P. Etienne, G. Creuzet, A. Friederich, and J. Chazelas, Giant Magnetoresistance of (001)Fe/(001)Cr Magnetic Superlattices, *Phys. Rev. Lett.* **61**, 2472 (1988).
- [3] G. Binasch, P. Grünberg, F. Saurenbach, and W. Zinn, Enhanced magnetoresistance in layered magnetic structures with antiferromagnetic interlayer exchange, *Phys. Rev. B* **39**, 4828 (1989).
- [4] R. A. Duine, K.-J. Lee, S. S. P. Parkin, and M. D. Stiles, Synthetic antiferromagnetic spintronics, *Nat. Phys.* **14**, 217 (2018).
- [5] J. Unguris, R. J. Celotta, and D. T. Pierce, Observation of Two Different Oscillation Periods in the Exchange Coupling of Fe/Cr/Fe(100), *Phys. Rev. Lett.* **67**, 140 (1991).
- [6] M. A. Ruderman and C. Kittel, Indirect exchange coupling of nuclear magnetic moments by conduction electrons, *Phys. Rev.* **96**, 99 (1954).
- [7] T. Kasuya, A theory of metallic ferro- and antiferromagnetism on Zener’s model, *Prog. Theor. Phys.* **16**, 45 (1956).
- [8] K. Yosida, Magnetic properties of Cu-Mn alloys, *Phys. Rev.* **106**, 893 (1957).
- [9] P. Grünberg, R. Schreiber, Y. Pang, M. B. Brodsky, and H. Sowers, Layered Magnetic Structures: Evidence for Antiferromagnetic Coupling of Fe Layers across Cr Interlayers, *Phys. Rev. Lett.* **57**, 2442 (1986).
- [10] S. S. P. Parkin, N. More, and K. P. Roche, Oscillations in Exchange Coupling and Magnetoresistance in Metallic Superlattice Structures: Co/Ru, Co/Cr, and Fe/Cr, *Phys. Rev. Lett.* **64**, 2304 (1990).
- [11] S. S. P. Parkin, Systematic Variation of the Strength and Oscillation Period of Indirect Magnetic Exchange Coupling through the $3d$, $4d$, and $5d$ Transition Metals, *Phys. Rev. Lett.* **67**, 3598 (1991).
- [12] J. Hayakawa, S. Ikeda, Y. M. Lee, R. Sasaki, T. Meguro, F. Matsukura, H. Takahashi, and H. Ohno, Current-induced magnetization switching in MgO barrier based magnetic tunnel junctions with CoFeB/Ru/CoFeB synthetic ferrimagnetic free layer, *Jpn. J. Appl. Phys.* **45**, L1057 (2006).
- [13] S. Parkin, J. Xin, C. Kaiser, A. Panchula, K. Roche, and M. Samant, Magnetically engineered spintronic sensors and memory, *Proc. IEEE* **91**, 661 (2003).
- [14] N. Smith, S. Maat, M. J. Carey, and J. R. Childress, Coresonant Enhancement of Spin-Torque Critical Currents in Spin Valves with a Synthetic-Ferrimagnet Free Layer, *Phys. Rev. Lett.* **101**, 247205 (2008).
- [15] S.-W. Lee and K.-J. Lee, Current-induced magnetization switching of synthetic antiferromagnetic free layer in magnetic tunnel junctions, *J. Appl. Phys.* **109**, 07C904 (2011).
- [16] A. Bergman, B. Skubic, J. Hellsvik, L. Nordström, A. Delin, and O. Eriksson, Ultrafast switching in a synthetic antiferromagnetic magnetic random-access memory device, *Phys. Rev. B* **83**, 224429 (2011).
- [17] D. Houssameddine, J. F. Sierra, D. Gusakova, B. Delaet, U. Ebels, L. D. Buda-Prejbeanu, M. C. Cyrille, B. Dieny, B. Ocker, J. Langer, and W. Maas, Spin torque driven excitations in a synthetic antiferromagnet, *Appl. Phys. Lett.* **96**, 072511 (2010).
- [18] J. L. Leal and M. H. Kryder, Unshielded spin valve heads exchange biased by synthetic antiferromagnets, *IEEE Trans. Magn.* **35**, 800 (1999).
- [19] S. Bandiera, R. C. Sousa, Y. Dahmane, C. Ducruet, C. Portemont, V. Baltz, S. Auffret, I. L. Prejbeanu, and B. Dieny, Comparison of synthetic antiferromagnets and hard ferromagnets as reference layer in magnetic tunnel junctions with perpendicular magnetic anisotropy, *IEEE Magnetics Letters* **1**, 3000204 (2010).
- [20] J. Chatterjee, S. Auffret, R. Sousa, P. Coelho, I.-L. Prejbeanu, and B. Dieny, Novel multifunctional RKKY coupling layer for ultrathin perpendicular synthetic antiferromagnet, *Sci. Rep.* **8**, 11724 (2018).
- [21] S.-H. Yang, K.-S. Ryu, and S. Parkin, Domain-wall velocities of up to 750 m s^{-1} driven by exchange-coupling torque in synthetic antiferromagnets, *Nat. Nanotechnol.* **10**, 221 (2015).
- [22] S.-H. Yang, C. Garg, and S. S. P. Parkin, Chiral exchange drag and chirality oscillations in synthetic antiferromagnets, *Nat. Phys.* **15**, 543 (2019).
- [23] T. Dohi, S. DuttaGupta, S. Fukami, and H. Ohno, Formation and current-induced motion of synthetic antiferromagnetic skyrmion bubbles, *Nat. Commun.* **10**, 5153 (2019).
- [24] W. Legrand, D. Maccariello, F. Ajejas, S. Collin, A. Vecchiola, K. Bouzehouane, N. Reyren, V. Cros, and A. Fert, Room-temperature stabilization of antiferromagnetic skyrmions in synthetic antiferromagnets, *Nat. Mater.* **19**, 34 (2020).
- [25] D.-S. Han, K. Lee, J.-P. Hanke, Y. Mokrousov, K.-W. Kim, W. Yoo, Y. L. W. van Hees, T.-W. Kim, R. Lavrijsen, C.-Y. You, H. J. M. Swagten, M.-H. Jung, and M. Kläui, Long-range chiral exchange interaction in synthetic antiferromagnets, *Nat. Mater.* **18**, 703 (2019).
- [26] A. Fernández-Pacheco, E. Vedmedenko, F. Ummelen, R. Mansell, D. Petit, and R. P. Cowburn, Symmetry-breaking interlayer Dzyaloshinskii–Moriya interactions in synthetic antiferromagnets, *Nat. Mater.* **18**, 679 (2019).
- [27] E. Y. Vedmedenko, P. Riego, J. A. Arregi, and A. Berger, Interlayer Dzyaloshinskii–Moriya Interactions, *Phys. Rev. Lett.* **122**, 257202 (2019).
- [28] C. Bi, H. Almasi, K. Price, T. Newhouse-Illige, M. Xu, S. R. Allen, X. Fan, and W. Wang, Anomalous spin-orbit torque

- switching in synthetic antiferromagnets, *Phys. Rev. B* **95**, 104434 (2017).
- [29] P. X. Zhang, L. Y. Liao, G. Y. Shi, R. Q. Zhang, H. Q. Wu, Y. Y. Wang, F. Pan, and C. Song, Spin-orbit torque in a completely compensated synthetic antiferromagnet, *Phys. Rev. B* **97**, 214403 (2018).
- [30] Y. Ishikuro, M. Kawaguchi, T. Taniguchi, and M. Hayashi, Highly efficient spin-orbit torque in Pt/Co/Ir multilayers with antiferromagnetic interlayer exchange coupling, *Phys. Rev. B* **101**, 014404 (2020).
- [31] Z. R. Nunn, C. Abert, D. Suess, and E. Girt, Control of the noncollinear interlayer exchange coupling, *Sci. Adv.* **6**, eabd8861 (2020).
- [32] C.-H. Chang, K.-P. Dou, Y.-C. Chen, T.-M. Hong, and C.-C. Kaun, Engineering the interlayer exchange coupling in magnetic trilayers, *Sci. Rep.* **5**, 16844 (2015).
- [33] P. Bruno, Oscillations of interlayer exchange coupling vs. ferromagnetic-layers thickness, *Europhysics Letters (EPL)* **23**, 615 (1993).
- [34] M. Stier and W. Nolting, Carrier-mediated interlayer exchange, ground-state phase diagrams, and transition temperatures of magnetic thin films, *Phys. Rev. B* **84**, 094417 (2011).
- [35] S. Blizak, G. Bihlmayer, S. Blügel, and S. E. H. Abaidia, Interlayer exchange coupling between FeCo and Co ultrathin films through Rh(001) spacers, *Phys. Rev. B* **91**, 014408 (2015).
- [36] J. Barnaś, Coupling between two ferromagnetic films through a non-magnetic metallic layer, *J. Magn. Magn. Mater.* **111**, L215 (1992).
- [37] S. N. Okuno and K. Inomata, Oscillatory exchange coupling with a period of two Fe monolayers in Au/Fe/Au/Fe/Au(001), *Phys. Rev. B* **51**, 6139 (1995).
- [38] P. J. H. Bloemen, M. T. Johnson, M. T. H. van de Vorst, R. Coehoorn, J. J. de Vries, R. Jungblut, J. Aan de Stegge, A. Reinders, and W. J. M. de Jonge, Magnetic Layer Thickness Dependence of the Interlayer Exchange Coupling in (001)Co/Cu/Co, *Phys. Rev. Lett.* **72**, 764 (1994).
- [39] S. N. Okuno and K. Inomata, Two Oscillatory Behaviors as Functions of Ferromagnetic Layer Thickness in Fe/Cr(100) Multilayers, *Phys. Rev. Lett.* **72**, 1553 (1994).
- [40] L. Li, D. Han, W. Lei, Z. Liu, F. Zhang, X. Mao, P. Wang, and H. Hou, Interlayer exchange coupling in $[\text{Pt}/\text{Co}]_n/\text{MgO}/[\text{Co}/\text{Pt}]_2$ perpendicular magnetic tunnel junctions, *J. Appl. Phys.* **116**, 123904 (2014).
- [41] P. Bruno and C. Chappert, Oscillatory Coupling between Ferromagnetic Layers Separated by a Nonmagnetic Metal Spacer, *Phys. Rev. Lett.* **67**, 1602 (1991).
- [42] P. Bruno and C. Chappert, Ruderman-Kittel theory of oscillatory interlayer exchange coupling, *Phys. Rev. B* **46**, 261 (1992).
- [43] P. Bruno, Interlayer exchange coupling: A unified physical picture, *J. Magn. Magn. Mater.* **121**, 248 (1993).
- [44] M. D. Stiles, Exchange coupling in magnetic heterostructures, *Phys. Rev. B* **48**, 7238 (1993).
- [45] P. Bruno, Theory of interlayer magnetic coupling, *Phys. Rev. B* **52**, 411 (1995).
- [46] R. Lavrijsen, A. Fernández-Pacheco, D. Petit, R. Mansell, J. H. Lee, and R. P. Cowburn, Tuning the interlayer exchange coupling between single perpendicularly magnetized CoFeB layers, *Appl. Phys. Lett.* **100**, 052411 (2012).
- [47] K. Wang, L. Qian, S.-C. Ying, and G. Xiao, Manipulation of the interlayer exchange coupling in perpendicular magnetized thin films via tunable magnetic-layer and spacer thicknesses, *Phys. Rev. B* **102**, 144430 (2020).
- [48] M. S. Gabor, T. Petrisor, R. B. Mos, M. Nasui, C. Tiusan, and T. Petrisor, Interlayer exchange coupling in perpendicularly magnetized Pt/Co/Ir/Co/Pt structures, *J. Phys. D: Appl. Phys.* **50**, 465004 (2017).
- [49] Q. Ma, Y. Li, Y.-S. Choi, W.-C. Chen, S. J. Han, and C. L. Chien, Spin orbit torque switching of synthetic Co/Ir/Co trilayers with perpendicular anisotropy and tunable interlayer coupling, *Appl. Phys. Lett.* **117**, 172403 (2020).
- [50] T. Xu, H.-A. Zhou, Y. Dong, Q. Zhang, M. Che, L. Liu, Z. Wu, Z. Guan, L. Yang, and W. Jiang, Fully Compensated Synthetic Antiferromagnets with Pronounced Anomalous Hall and Magneto-Optical Responses, *Phys. Rev. Appl.* **16**, 044056 (2021).
- [51] A. Barla, J. Nicolas, D. Cocco, S. M. Valvidares, J. Herrero-Martin, P. Gargiani, J. Moldes, C. Ruget, E. Pellegrin, and S. Ferrer, Design and performance of BOREAS, the beamline for resonant x-ray absorption and scattering experiments at the ALBA synchrotron light source, *J. Synchrotron Radiat.* **23**, 1507 (2016).
- [52] J. Finley and L. Liu, Spin-Orbit-Torque Efficiency in Compensated Ferrimagnetic Cobalt-Terbium Alloys, *Phys. Rev. Appl.* **6**, 054001 (2016).
- [53] R. Mishra, J. Yu, X. Qiu, M. Motapothula, T. Venkatesan, and H. Yang, Anomalous Current-Induced Spin Torques in Ferrimagnets near Compensation, *Phys. Rev. Lett.* **118**, 167201 (2017).
- [54] Y. Dong, T. Xu, H.-A. Zhou, L. Cai, H. Wu, J. Tang, and W. Jiang, Electrically reconfigurable 3D spin-orbitronics, *Adv. Funct. Mater.* **31**, 2007485 (2021).
- [55] Z. Zhang, L. Zhou, P. E. Wigen, and K. Ounadjela, Angular dependence of ferromagnetic resonance in exchange-coupled Co/Ru/Co trilayer structures, *Phys. Rev. B* **50**, 6094 (1994).
- [56] See the Supplemental Material at <http://link.aps.org/supplemental/10.1103/PhysRevApplied.18.054051> for additional information on micromagnetic simulation, experimental realization of the first type of SAF, evolutions of coercive fields, and AFM exchange-coupling fields as a function of Fe-Tb thickness.
- [57] A. Fert, V. Cros, and J. Sampaio, Skyrmions on the track, *Nat. Nanotechnol.* **8**, 152 (2013).
- [58] P. J. Metaxas, J. P. Jamet, A. Mougin, M. Cormier, J. Ferré, V. Baltz, B. Rodmacq, B. Dieny, and R. L. Stamps, Creep and Flow Regimes of Magnetic Domain-Wall Motion in Ultrathin Pt/Co/Pt Films with Perpendicular Anisotropy, *Phys. Rev. Lett.* **99**, 217208 (2007).
- [59] Y. Mimura and N. Imamura, Magnetic properties of amorphous Tb-Fe thin films prepared by rf sputtering, *Appl. Phys. Lett.* **28**, 746 (1976).
- [60] P. Hansen, C. Clausen, G. Much, M. Rosenkranz, and K. Witter, Magnetic and magneto-optical properties of rare-earth transition-metal alloys containing Gd, Tb, Fe, Co, *J. Appl. Phys.* **66**, 756 (1989).
- [61] Y. Mimura, N. Imamura, and T. Kobayashi, Magnetic properties and curie point writing in amorphous metallic films, *IEEE Trans. Magn.* **12**, 779 (1976).

- [62] O. Hellwig, A. Berger, J. B. Kortright, and E. E. Fullerton, Domain structure and magnetization reversal of antiferromagnetically coupled perpendicular anisotropy films, *J. Magn. Magn. Mater.* **319**, 13 (2007).
- [63] E. N. Welbourne, T. Vemulkar, D. C. M. C. Petit, and R. P. Cowburn, Weakly coupled synthetic antiferromagnetic nanodisks with perpendicular magnetic anisotropy for lab-on-chip devices, *Appl. Phys. Lett.* **119**, 102401 (2021).
- [64] Y. Saito, S. Ikeda, and T. Endoh, Synthetic antiferromagnetic layer based on Pt/Ru/Pt spacer layer with 1.05 nm interlayer exchange oscillation period for spin-orbit torque devices, *Appl. Phys. Lett.* **119**, 142401 (2021).
- [65] R. B. Morgunov, A. V. Yurov, V. A. Yurov, A. D. Talantsev, A. I. Bezverhni, and O. V. Koplak, Oscillatory dynamics of the magnetic moment of a Pt/Co/Ir/Co/Pt synthetic antiferromagnet, *Phys. Rev. B* **100**, 144407 (2019).
- [66] Z. Q. Qiu, J. Pearson, and S. D. Bader, Oscillatory interlayer magnetic coupling of wedged Co/Cu/Co sandwiches grown on Cu(100) by molecular beam epitaxy, *Phys. Rev. B* **46**, 8659 (1992).
- [67] Z. Q. Qiu, J. Pearson, A. Berger, and S. D. Bader, Short-Period Oscillations in the Interlayer Magnetic Coupling of Wedged Fe(100)/Mo(100)/Fe(100) Grown on Mo(100) by Molecular-Beam Epitaxy, *Phys. Rev. Lett.* **68**, 1398 (1992).
- [68] R. Q. Zhang, *et al.*, Current-induced magnetization switching in a CoTb amorphous single layer, *Phys. Rev. B* **101**, 214418 (2020).
- [69] S. Krishnia, E. Haltz, L. Berges, L. Aballe, M. Foerster, L. Bocher, R. Weil, A. Thiaville, J. Sampaio, and A. Mougin, Spin-Orbit Coupling in Single-Layer Ferrimagnets: Direct Observation of Spin-Orbit Torques and Chiral Spin Textures, *Phys. Rev. Appl.* **16**, 024040 (2021).
- [70] Q. Liu, L. Zhu, X. S. Zhang, D. A. Muller, and D. C. Ralph, Giant bulk spin-orbit torque and efficient electrical switching in single ferrimagnetic FeTb layers with strong perpendicular magnetic anisotropy, *Appl. Phys. Rev.* **9**, 021402 (2022).
- [71] C. O. Avci, C.-H. Lambert, G. Sala, and P. Gambardella, Chiral Coupling between Magnetic Layers with Orthogonal Magnetization, *Phys. Rev. Lett.* **127**, 167202 (2021).